



Complex Nano-objects Displaying Both Magnetic and Catalytic Properties: A Proof of Concept for Magnetically Induced Heterogeneous Catalysis

Anca Meffre, Boubker Mehdaoui, Vincent Connord, Julian Carrey, Pier-Francesco Fazzini, Sébastien Lachaize, Marc Respaud, Bruno Chaudret

► To cite this version:

Anca Meffre, Boubker Mehdaoui, Vincent Connord, Julian Carrey, Pier-Francesco Fazzini, et al.. Complex Nano-objects Displaying Both Magnetic and Catalytic Properties: A Proof of Concept for Magnetically Induced Heterogeneous Catalysis. Nano Letters, 2015, 15 (5), pp.3241-3248. hal-02020314

HAL Id: hal-02020314

<https://insa-toulouse.hal.science/hal-02020314v1>

Submitted on 2 Jan 2025

HAL is a multi-disciplinary open access archive for the deposit and dissemination of scientific research documents, whether they are published or not. The documents may come from teaching and research institutions in France or abroad, or from public or private research centers.

L'archive ouverte pluridisciplinaire **HAL**, est destinée au dépôt et à la diffusion de documents scientifiques de niveau recherche, publiés ou non, émanant des établissements d'enseignement et de recherche français ou étrangers, des laboratoires publics ou privés.

Complex nano-objects displaying both magnetic and catalytic properties:

A proof of concept for magnetically induced heterogeneous catalysis

Anca Meffre¹, Boubker Mehdaoui¹, Vincent Connord¹, Julian Carrey¹, Pier Francesco Fazzini¹,
Sébastien Lachaize¹, Marc Respaud^{1*}, Bruno Chaudret^{1*}

¹Laboratoire de Physique et Chimie des Nano Objets, LPCNO, UMR5215 INSA-UPS-CNRS,
Université de Toulouse; Institut National des Sciences Appliquées, 135 avenue de Rangueil,
31077 Toulouse, France

*e-mail : bruno.chaudret@insa-toulouse.fr; marc.respaud@insa-toulouse.fr;

Abstract:

Addition of $\text{Co}_2(\text{Co})_9$ and $\text{Ru}_3(\text{CO})_{12}$ on preformed monodisperse iron(0) nanoparticles (Fe(0) NPs) at 150°C under H_2 leads respectively to monodisperse core-shell Fe@FeCo NPs and to a thin discontinuous Ru(0) layer supported on the initial Fe(0) NPs. The new complex NPs were studied by state-of-the-art transmission electron microscopy techniques as well as X-ray diffraction, Mössbauer spectroscopy and magnetic measurements. These particles display large heating powers (SAR) when placed in an alternating magnetic field. The combination of magnetic and surface catalytic properties of these novel objects were used to demonstrate a new concept: the possibility of performing Fischer-Tropsch Syntheses by heating the catalytic nanoparticles with an external alternating magnetic field.

Keywords : Magnetic Nanoparticle, Iron, Bimetallic, Catalysis, Fischer-Tropsch

Introduction

Fossil energy shortage urges for the increase in the use of renewable energy as well as for the development of new approaches to minimize energy consumption. However, energy storage remains the main problem and even if several options are presently studied such as electrochemical storage (batteries), hydrogen production, heat production etc...¹ The so called power to gas or power to liquid approaches, is based on hydrocarbon synthesis. It is still the best present option, i.e. because of the compatibility of hydrocarbons with current usages and their high energy density. The main artificial preparation routes of hydrocarbons involve the hydrogenation of CO, named Fischer Tropsch Syntheses (FTS), a catalytic process occurring in the range 200-500°C.²⁻¹⁰ Typical Fischer-Tropsch catalysts consist in iron nanoparticles dispersed on a support (in general alumina powder).⁴

An alternative and attractive solution for thermal heating is magnetic induction, which consists in using the eddy currents and/or hysteresis losses induced in metals and ferromagnetic materials respectively by high-frequency alternating magnetic fields. Magnetic induction shows several advantages when compared to other heating techniques, the main one being the simplicity since this is a non-contact method. From the energetic point of view, it displays the highest power transmission¹¹ since the energy is directly transferred inside the material to be heated. Combined with very short warming times, magnetic heating is thus very energetically efficient and, consequently, often employed for daily life and industrial applications. The heating efficiency is characterized by the specific absorption rate (SAR) of the material. Pioneering results on the use of magnetic nanoparticles to heat reaction solutions by induction have been obtained by Kirschning's group, evidencing that numerous chemical reactions in liquid media can be

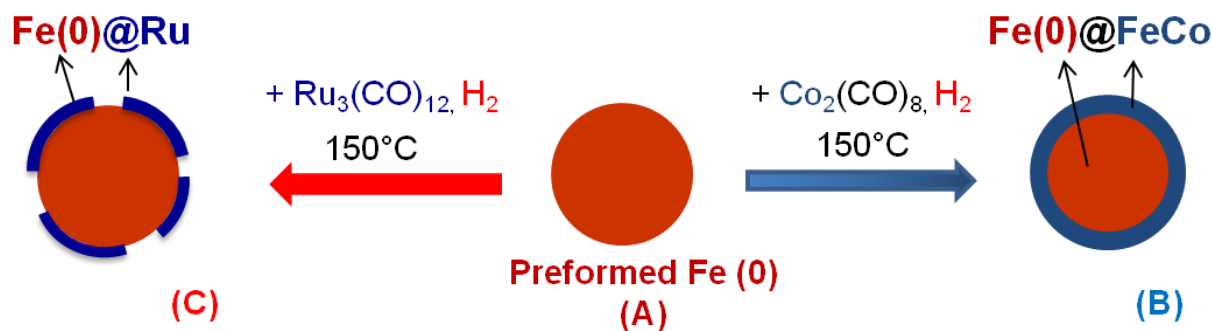
triggered using heating induced by iron oxide nanoparticles.¹²⁻¹⁵ For that purpose, his group designed continuous flow reactors, allowing to perform for instance multi step flow synthesis, and reactions in solution using functionalized MagSilica® with Pd nanoparticles as catalyst.¹² Interesting results also come from the field of nanomedicine, which aims at using the heat generated in magnetic nanoparticles to kill cancer cells – the so-called magnetic hyperthermia –, or to release drug from liposomes.¹⁶⁻²¹ Along their basic research in this field, several groups have demonstrated that the heat generated by induction is able to induce chemical reactions at their surface: molecule cleaving^{16,17}, DNA denaturing¹⁸, polymer transition¹⁹, fluorescence quenching²⁰, or cell death²¹. So far, the reaction temperature is limited almost well below the 200°C limit, as a result of the limited SAR of iron oxide nanoparticles. To the best of our knowledge, magnetic heating has not yet been used to heat selectively heterogeneous catalysts at high temperature, a prerequisite condition to perform e.g. Fischer Tropsch Syntheses. Using a high SAR heterogeneous catalysts heated by induction would present several advantages: i) at the nanometer scale, induction heating is almost instantaneous, which can allow the conversion process to be instantaneously switched on or off to follow intermittent energy production; ii) the catalyst support, if any, and the entire reactor, would not need to be heated, which would save a considerable amount of energy; iii) energy transfer would result from induction, i.e. would be far better than conduction, since heating would come from inside the catalyst and not outside from the reactor. Putting all these points together, it is not unreasonable to imagine developing a “cold catalysis”, where minor amounts of energy would be injected to induce a high catalytic reaction. Using magnetically heated NPs for power-to-hydrocarbons conversion is however challenging since there is presently no available nano-objects displaying at the same time large heating power in alternating magnetic fields and good catalytic properties for CO hydrogenation. Moreover, since Fischer-Tropsch reactions occur above 200°C, a specific design of catalyst is necessary to

keep heating and catalytic properties stable during the reaction. To date, the most efficient catalysts for these processes are based on ruthenium metal²²⁻²⁴, which remains very expensive, while real processes use iron^{25,26} and cobalt-based²⁷ catalysts. Tailoring catalysts for a specific FTS “cold catalysis” requires the exploration of new magnetic catalysts that combine a ferromagnetic core displaying a large inductive performance (high SAR) with a highly catalytic surface. This represents a real challenge since the reaction occurs in a relatively narrow temperature window: no reaction occurs at low temperature while only carbon forms at too high temperature. Moreover, it is known that in real processes, the catalysts have a tendency to coalesce and their chemical composition changes from iron to iron carbide.

In our group we have developed for the past ten years the synthesis and characterization of Fe(0) NPs, displaying a high monodispersity, an adjustable size, a controlled surface and good magnetic properties, in particular a saturation magnetization (M_s) very close to that of bulk iron.^{28,29} A fine control of the size and composition of these particles has allowed to reach very large heating powers in a small alternating magnetic field.³⁰⁻³² In order to meet the challenges associated to combining magnetic heating and catalysis, we have considered varying the size of the Fe(0) NPs, and have selectively doped their surface with cobalt or ruthenium, two metals known to be efficient FTS catalysts. We report hereafter the demonstration of the possibility to combine magnetic heating and heterogeneous catalytic properties in a model system involving core-shell magnetic NPs for CO hydrogenation. This includes: i) the first versatile chemical synthesis of monodisperse core@shell iron@iron-cobalt and ruthenium on iron(0) nanoparticles, both of controlled size and composition and ii) the optimization of the catalytic properties of these new nano-objects while keeping high heating powers and hence leading to the proof of concept of a “cold FTS process”

Results and discussion

For the synthesis of the bimetallic nano-objects, we have adapted the previously reported route towards iron carbide NPs.³² It consists in a two-step procedure based on: (a) synthesis of iron(0) NPs and (b) decomposition of a carbonyl derivative of Co or Ru on these preformed iron(0) NPs under H_2 (see Scheme 1). First, Fe(0) NPs are obtained with very good yields through the decomposition of the organometallic complex $\{Fe[N(SiMe_3)_2]_2\}_2$ in the presence of a mixture of hexadecylamine (HDA) and the corresponding ammonium chloride (HDAHCl) in mesitylene. By varying the reaction conditions, the size of these pure metallic Fe(0) nanoparticles is found between 8 and 12 nm.³³ Addition of 0.2 eq. $Co_2(CO)_8$ or 0.2 eq. $Ru_3(CO)_{12}$ to a mesitylene solution of *ca.* 11 nm preformed Fe(0) NPs (**1**) (See Figure S1) followed by heating at 150°C under 3 bars H_2 and vigorous magnetic stirring produces a magnetic black material sticking on the stirring bar. The black solution was removed, and the magnetic material collected after washing with toluene and drying *in vacuo*. Mass spectrometry monitoring evidenced in each case the formation of methane together with very small amounts of ethane and propane, as a result of hydrogenation of the carbonyl ligands of the cobalt and ruthenium precursors (See Figure S2).



Scheme 1: Typical synthesis of Fe@FeCo (B) and Fe@Ru (C) nanoparticles starting from preformed Fe(0) (A) nanoparticles.

As shown on Figure 1a and Figure 2a, the reactions lead to Fe@FeCo (**B**) and Fe@Ru (**C**) NPs of ca. 12.2 nm, respectively 12.4 nm, homogeneous in shape and size ($\sigma = 0.9$ nm for Fe@FeCo NPs and 0.6 nm for Fe@Ru NPs).

NPs **B** and **C** were analyzed by a series of structural and spectroscopic studies. First, TEM images evidenced a size increase of ca. 1 nm for both Fe@FeCo (**B**) and Fe@Ru (**C**) (see Figure 1a and Figure 2a). For both series of samples, XRD only showed the presence of the Fe *bcc* structure, which, in the case of (**B**) cannot be discriminated from that of the FeCo *bcc* alloy (see Figure 1d and Figure 2d).

The bimetallic structure of Fe@FeCo and Fe@Ru NPs was confirmed by combining High Resolution Transmission Electron Microscopy (HRTEM), Energy Dispersive X-Ray (EDX) mapping analysis (see Figure 1b,c and Figure 2b,c) and Mössbauer spectroscopy (see Figure 1e and Figure 2e). EDX mapped images of (**B**) and (**C**) demonstrate the presence of both Fe and Co on one side and both Fe and Ru on the other in one particle in relative 7.1% Co Fe@FeCo (**B**) and 6.7% Ru for Fe@Ru (**C**). This ratio is in agreement with the value obtained by elemental analysis. HRTEM and High Angle Annular Dark Field (HAADF) electron microscopy studies are consistent with the presence of an iron core and ruthenium on the surface in the case of Fe@Ru (**C**). For Fe@FeCo (**B**), the similar contrasts of Fe and Co and the similar structures of bulk Fe and FeCo do not allow any discrimination of the metals by this technique.

The analysis of the Mössbauer spectra, collected at 4.2 K, reveals the presence of Co and Ru, through a high hyperfine field contribution corresponding to a FeCo alloy,³⁴ and a low hyperfine field distribution corresponding to a FeRu alloy or Fe/Ru interface respectively (see Table S1 for the fitting parameters). In both cases, no evidence of carburization was found, in contrast to the

addition of $\text{Fe}(\text{CO})_5$ on preformed $\text{Fe}(0)$ NPs which led to iron carbide NPs. In the present case the iron(0) core is preserved after the decomposition of $\text{Co}_2(\text{CO})_8$ and $\text{Ru}_3(\text{CO})_{12}$ (see Figure 1e and Figure 2e). The difference lies presumably in the much better catalytic performances of cobalt and ruthenium at 150°C which allow the fast formation of hydrocarbons and thus prevent the formation of surface carbides. Note that, after CO addition, Fe@Ru nanoparticles clearly show in their IR spectra bands associated with CO coordination on ruthenium in a terminal (2052 cm^{-1}) and bridging mode ($1976, 1929\text{ cm}^{-1}$). By comparison, no CO stretch was observed after similar treatment of pure $\text{Fe}(0)$ NPs (See Figure S3)

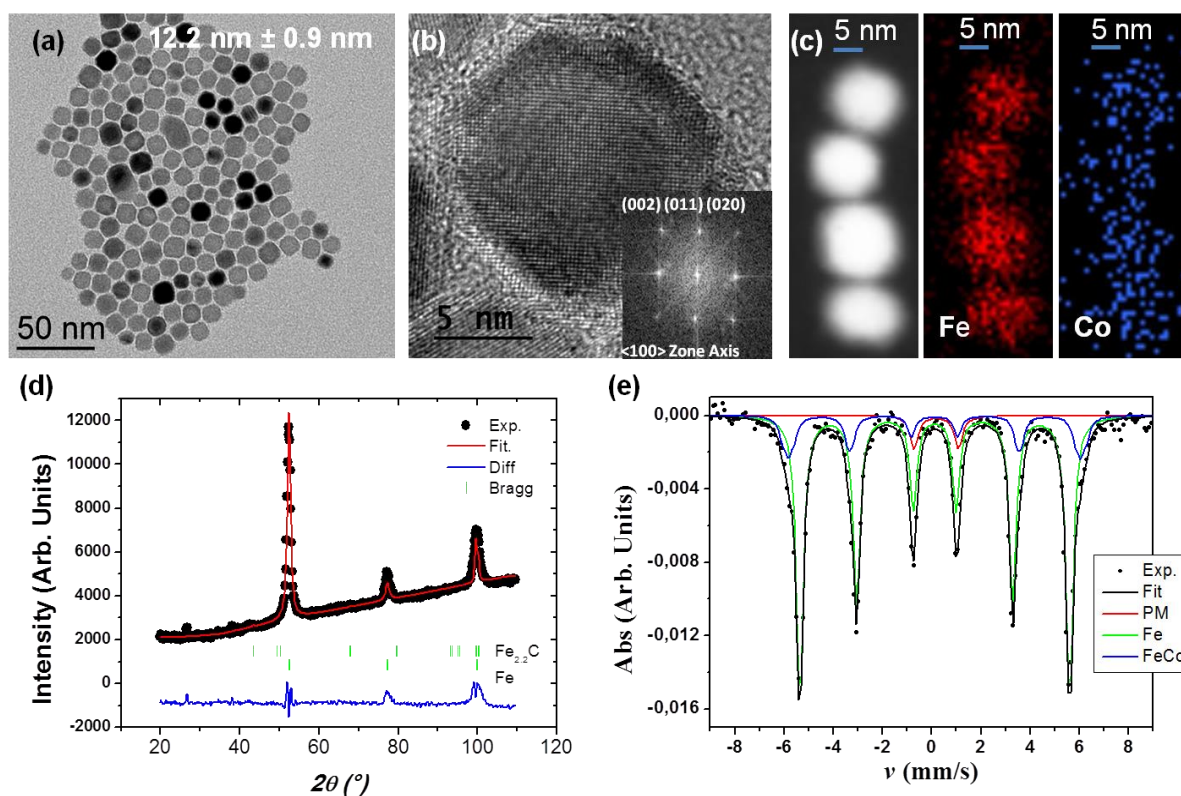


Figure 1: Structural analysis of Fe@FeCo nanocrystals (**B**) of about 12.2 nm. (a) TEM analysis of (**B**). (b) HRTEM analysis of (**B**). (c) EDX data of (**B**). (d) XRD pattern of (**B**). (e) Mössbauer spectrum of (**B**)

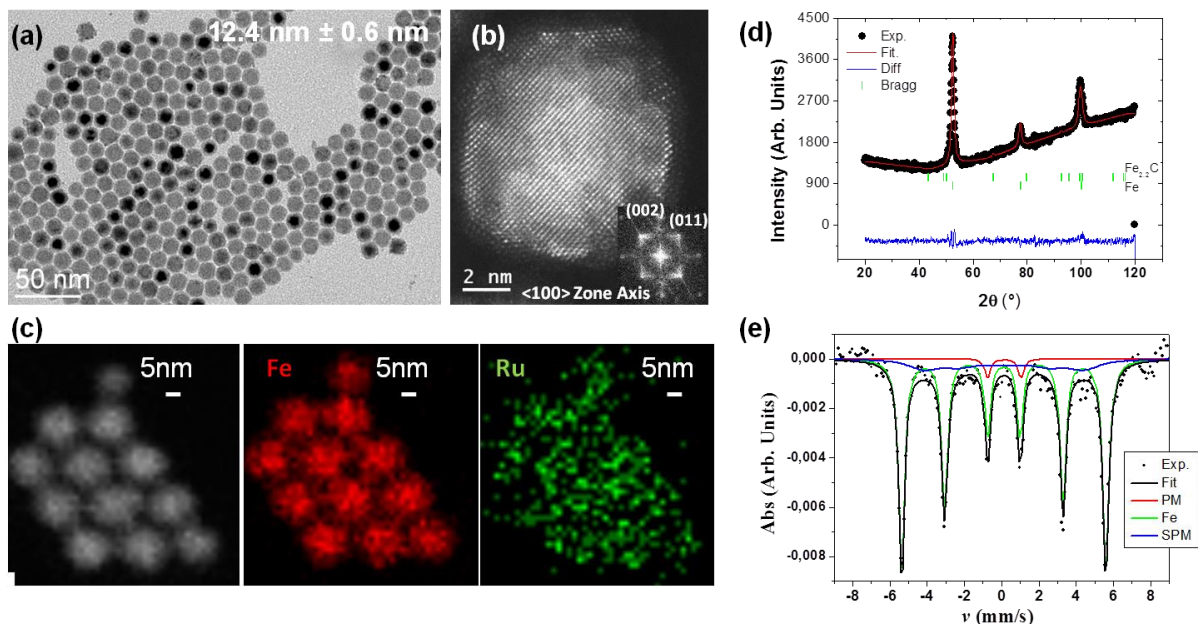


Figure 2: Structural analysis of Fe@Ru nanocrystals (C) of about 12.4 nm. (a) TEM analysis of (C). (b) HRTEM analysis of (C). (c) EDX data of (C). (d) XRD pattern of (C). (e) Mössbauer spectrum of (C).

Following this synthesis procedure, the final size of nano-objects can be finely controlled by varying the average size of the initial Fe(0) nanocrystals, while keeping all the others parameters constant. Fe@FeCo and Fe@Ru NPs were obtained in the range size from about 10.0 nm to 13.0 nm. (See Figure S4, S5, S6, S7, S8, S9). The Co or Ru final atomic concentration varies between 4.7 and 12 % which implies the formation in the case of cobalt of a thin alloyed FeCo layer, or in the case of ruthenium of a discontinuous Ru layer on the surface of iron. The main parameters of each compound are summarized in Table 1.

Sample	Diameter (TEM) (± 0.2)	Structure HRTEM	Co or Ru content EDX (Atomic) (± 1)	SAR (W/g) (54 kHz, 50mT)		CO hydrogenation Complete Reaction	Catalyst after CO hydrogenation	
				L (± 5)	P (± 10)		TEM General aspect	DRX (± 3)
Fe@FeCo	10.3 nm	bcc Fe(0)	12%	64	48	No	Individual	bcc Fe(0) : 57% ϵ -Fe _{2.2} C : 43%
Fe@FeCo (B)	12 nm	bcc Fe(0)	7.1%	284	64	No	Aggregates	bcc Fe(0) : 41% ϵ -Fe _{2.2} C : 59%
Fe@Ru	11.7 nm	bcc Fe(0)	4.7%	80	28	Yes	Individual	bcc Fe(0) : 67% ϵ -Fe _{2.2} C : 33%
Fe@Ru (C)	12.4 nm	bcc Fe(0)	6.7%	190	29	Yes	Individual	ϵ -Fe _{2.2} C : 100%

Table 1: Main characteristics of the nanoparticles: size, structural and chemical properties, SAR measured in mesitylene (L) and in powder (P), apparent catalytic activity and structural properties after catalysis.

Magnetic properties

The magnetic properties of the starting Fe(0) NPs (**A**) as well as those of Fe@FeCo NPs (**B**) and Fe@Ru NPs (**C**), were measured at 2 K and 300 K, with a superconducting quantum interference device model MPMS 5.5 SQUID magnetometer. The measurements were performed on dried powder samples prepared and sealed under argon atmosphere (glove box) to preserve them from uncontrolled oxidation. The absolute magnetization was deduced from the magnetic metal (0) content (Fe in the case of (**A**) and (**C**) and [Fe+Co] in the case of (**B**)) determined by microanalysis. As expected, the saturation magnetization (M_s) of preformed Fe(0) NPs is very close to that of bulk iron, 210 ($\pm 10\%$) Am²/kg at 2 K and 198 ($\pm 10\%$) Am²/kg at 300 K (See Figure S10). The saturation magnetization of (**B**) remains close to that of bulk iron 210 ($\pm 10\%$) Am²/kg at 2 K and 206 ($\pm 10\%$) Am²/kg at 300 K (See Figure S11). In contrast to (**B**), for (**C**), the presence of Ru on the surface, leads to a decrease of saturation magnetization down to about

170 ($\pm 10\%$) Am²/kg at 2 K and 165 ($\pm 10\%$) Am²/kg at 300 K (See Figure S12). It is interesting to note that NPs (A) and (C) exhibit a soft ferromagnetic behaviour at room temperature (coercive fields below 3mT), while (C) is very close to a superparamagnetic material (coercive fields below 1mT). Here, in contrast to Co, which normally induces a higher local magnetism, Ru plays a detrimental role for the local Fe magnetism.³⁵ As a consequence, the “effective magnetic size” is reduced, leading to a reduced saturation magnetization and coercive field for (C) as compared to (A) and (B).

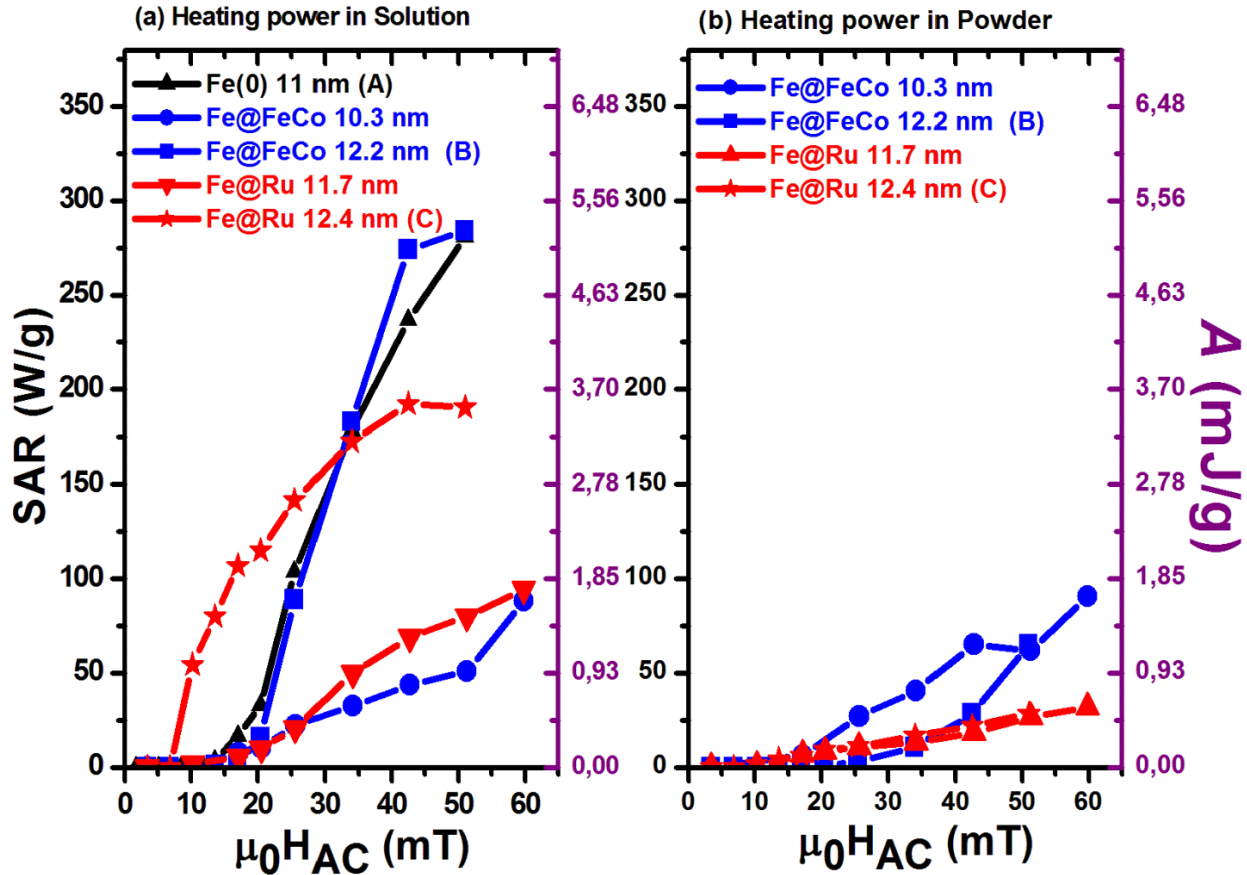


Figure 3: Heating power of iron based nanoparticles. SAR measurements at $f_{exc} = 54\text{kHz}$ of Fe(0) NPs of about 11.0 nm and two different sizes of Fe@FeCo and Fe@Ru NPs, measured in solution (a) and as powder (b). The energy losses per cycle A is also given.

The heating powers (SAR) generated by these nano-objects in an alternating magnetic field were determined by measuring the temperature rise of colloidal solutions upon applying an alternating magnetic field on a homemade frequency adjustable electromagnet according to a previously described method.^{30,31} The SAR dependence as a function of magnetic field measured at a frequency $f_{\text{exc}} = 54$ kHz is described for two representative samples of solution of **(B)** and **(C)** NPs in solution in mesitylene (see Figure 3a). SAR measurements of preformed metallic Fe(0) NPs **(A)** of 11 nm is also shown for the sake of comparison. As observed for metallic Fe(0) NPs,³¹ the bimetallic samples exhibit behaviours typical of NPs in the ferromagnetic regime, evidenced by the abrupt increase of SAR above a critical field ($\mu_0 H_{\text{crit.}}$), which may be followed by a saturation. Similarly to pure Fe(0) NPs, the SAR values increase with particle size. The larger Fe@Ru NPs combine a high SAR and a low $\mu_0 H_{\text{crit.}}$ which may be very interesting in the context of the use of a small applied magnetic field to minimize energy consumption. The larger Fe@FeCo NPs display a similar behaviour as Fe(0) NPs. These SAR values are correlated with the evolution of the spontaneous magnetization, which is reduced for Fe@Ru NPs. For the smallest NPs the power is smaller.

The SAR values of the corresponding powders (see Figure 3b), in the experimental conditions used for catalysis are generally lower than those measured in solution. The heating power seems to be correlated to the material, while the size plays a marginal role. High frequency measurements, performed both on solutions and powders, show that in the solid state hysteresis loops are closed and display a reduced remanence whereas in solution hysteresis loops display a much higher remanence. These behaviors result from a lower concentration of NPs in solution when compared to solid state and from the tendency of NPs to organize in solution into columns or chains upon application of a magnetic field as previously discussed.³⁶ Nevertheless, the

important point is that the heating power of these complex nanoparticles is preserved despite surface modification, with SAR values in the range of 65 W/g for Fe@FeCo (**B**) and 28 W/g Fe@Ru (**C**) at a frequency of 54 kHz and an amplitude of 50 mT. The SAR of (**C**) is probably reduced as a result of the presence of a less magnetic surface in the case of Ru.

Catalytic properties

The next step was to test these bimetallic iron based nanoparticles as heterogeneous catalysts, for CO hydrogenation, a reaction leading to Fischer-Tropsch Syntheses (FTS). The catalytic activities were tested in an alternating magnetic field, oscillating at a frequency of 54 kHz and an amplitude of 50 mT, in the conditions providing the maximum heating power. A typical catalytic reaction was carried out in a 4 ml Fischer-Porter bottle using 10 mg of nanoparticle powder containing ca 80 wt.% of metal, pressurized with 4 bars of a mixture $\text{H}_2/^{13}\text{CO} = 4$ in the absence of any solvent or support. The nanoparticle powder lies at the bottom of Fischer-Porter bottle and is exposed to the alternating magnetic field. ^{13}CO was used in order to: i) be able to monitor the reaction by gas phase NMR and ii) insure that the observed gas phase products find their origin in the added CO and not elsewhere, for example, in the decomposition of the remaining ligands. After 4 hours of reaction, CO conversion and product selectivity of the three catalysts were investigated by combining ^1H and ^{13}C gas NMR with mass spectrometry. For this purpose, the gas mixtures produced were transferred into Quick Pressure (QPV) NMR Sample tubes (0.77 mm wall thickness) closed with a Teflon needle valve, and then analysed.

First, the catalytic activity was tested on the starting Fe(0) NPs. Upon magnetic field application, the gas pressure immediately and slowly decreases down to 3 bars after 4 hours. As monitored by mass spectrometry and gas phase ^{13}C NMR a low conversion was achieved (see Figure 4c and Figure S13). These results were compared to those obtained for modified

nanoparticles: Fe@FeCo (**B**) and Fe@Ru (**C**). Compared to (**A**), the gas pressure decreases much faster, down to 1.5 bar and 1 bar for (**B**) and (**C**) respectively. The conversion is much more important in the case of (**B**) and complete for (**C**) (see Figures 4 and S13).

Concerning the selectivity, gas phase ^1H NMR allows to distinguish easily $^{13}\text{CH}_4$ which appears as a doublet at 0.2 ppm from $^{13}\text{CH}_3$ - and $^{13}\text{CH}_2$ groups of saturated higher hydrocarbons (ethane, propane, butane essentially) which show doublets at respectively 0.8 and 1.3 ppm (see Figure 4d). The spectrum obtained for (**C**) (see Figure 4d) almost only shows these latter features whereas mass spectrometry evidence the presence of C1 to C6 hydrocarbons (see Figure 4a). This result can therefore be interpreted as the formation of mainly saturated light hydrocarbons. The ^1H NMR spectra obtained in the case of (**B**) show a more complex pattern between 1 and 2.5 ppm together with additional peaks between 4.5 and 6.0 ppm indicative of the formation of olefins. Moreover, mass spectra evidence the presence in the case of (**B**) and pure Fe the presence of only light hydrocarbons (see Figure 4a, b). Finally, for pure Fe, some olefin peaks are masked by the broad dihydrogen signal centred at 4.6 ppm. However all these data show that the observed reactivity and of these nanoparticles are qualitatively comparable to that observed in real FTS: Ru is the most active and favours chain growth together with the formation of saturated hydrocarbons whereas the presence of iron leads to the formation of olefins.

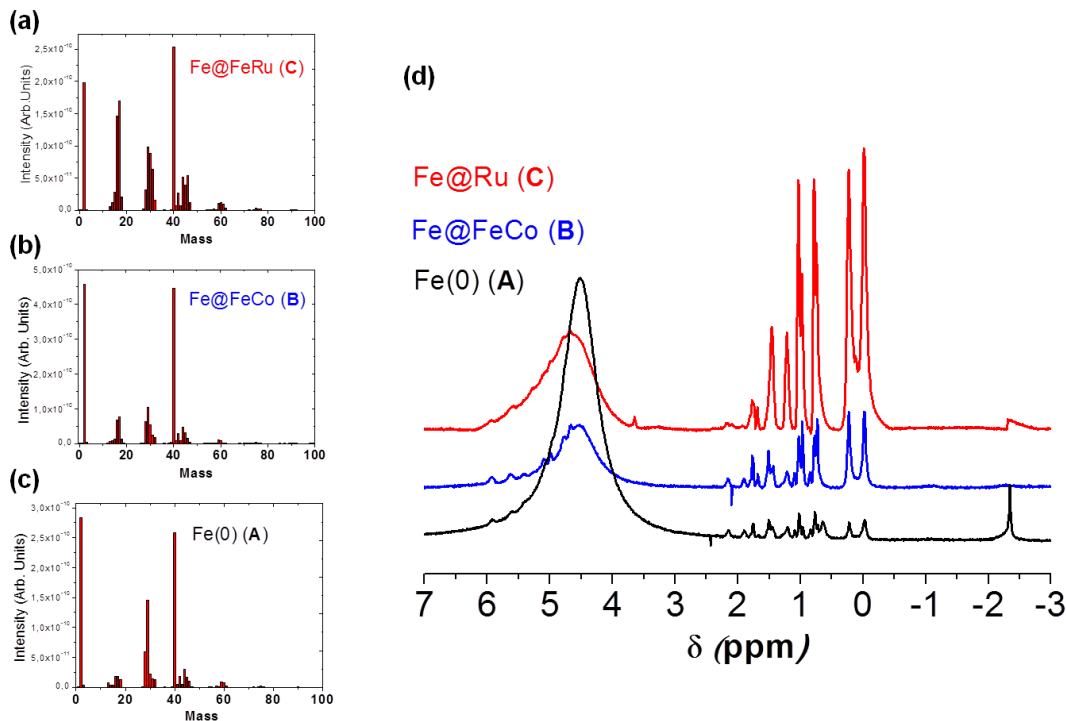


Figure 4: (a) mass spectra after FTS using (C); (b) mass spectra after FTS using (B); (c) mass spectra after FTS using (A) (d) ^1H gas NMR of the gas obtained after FTS using Fe(0) (A), Fe@FeCo (B) and Fe@Ru (C) as catalyst.

The same trends are also observed for smaller nanoparticles, a fast decrease of the pressure down to 1 bar and a complete conversion for Fe@Ru, while a slower decrease to 2 bars and an uncomplete conversion for the Fe@FeCo (see Figure S14, S15).

Two main reasons can explain the difference in the conversion: (i) kinetic of the reaction, and (ii) the degradation of the nanoparticles during the FTS. In order to understand the influence of the catalytic process on the catalysts, the structural properties of the 5 samples were examined using HRTEM, and DRX after catalysis (see Table S1). In the case of pure Fe(0) NPs, the general morphology is changed, with some aggregation of the nanoparticles and a concomitant increase in the particle size. A partial carburization is visible which consists in the formation of a carbon shell surrounding the particles, and evidence for partial transformation of Fe into crystalline

ϵ -Fe_{2.2}C (67% of ϵ -Fe_{2.2}C) (See Figure S16). In contrast, for Fe@Ru systems, as shown on Figure 5 no change in the particle size and overall morphology were observed but a total carburation of the core (Fe => ϵ -Fe_{2.2}C) for the larger particles system (12.4 nm), while the smaller (11.7 nm) remain partially preserved (67% of Fe(0) and 33% of ϵ -Fe_{2.2}C). The evolution of Fe@FeCo is intermediate between Fe(0) and Fe@Ru, with a change in their morphology and some size increase but without severe aggregation (See Figure S17). However, a carbide shell is again observed as well as partial carburation of the core into ϵ -Fe_{2.2}C, for both the larger ones) and the smaller ones (57% of Fe(0) and 43% of ϵ -Fe_{2.2}C for 10.3nm, and 41% of Fe(0) and 59% of ϵ -Fe_{2.2}C for 12nm). As previously reported for the synthesis of FeC nanoparticles, other Fe carbide phases may be also present, such as the Hagg phase χ -Fe₅C₂.³²

Thus, the apparent extended coalescence of the pure Fe nanoparticles and the formation of large quantities of carbon may result from a high temperature reached, thanks to the high SAR of these materials, associated to a weak catalytic efficiency, and may account for their prompt deactivation. By contrast, the low SAR of Fe@Ru may explain the conservation of the particles size and shape after catalysis. Moreover the higher activity of Ru allows faster carbon elimination, and prevents the surface from carburation. The case of Fe@FeCo is intermediate between Fe and Fe@Ru, high SAR, leading to particle aggregation, and to a relatively high catalytic activity which limits the carbon poisoning of the surface.

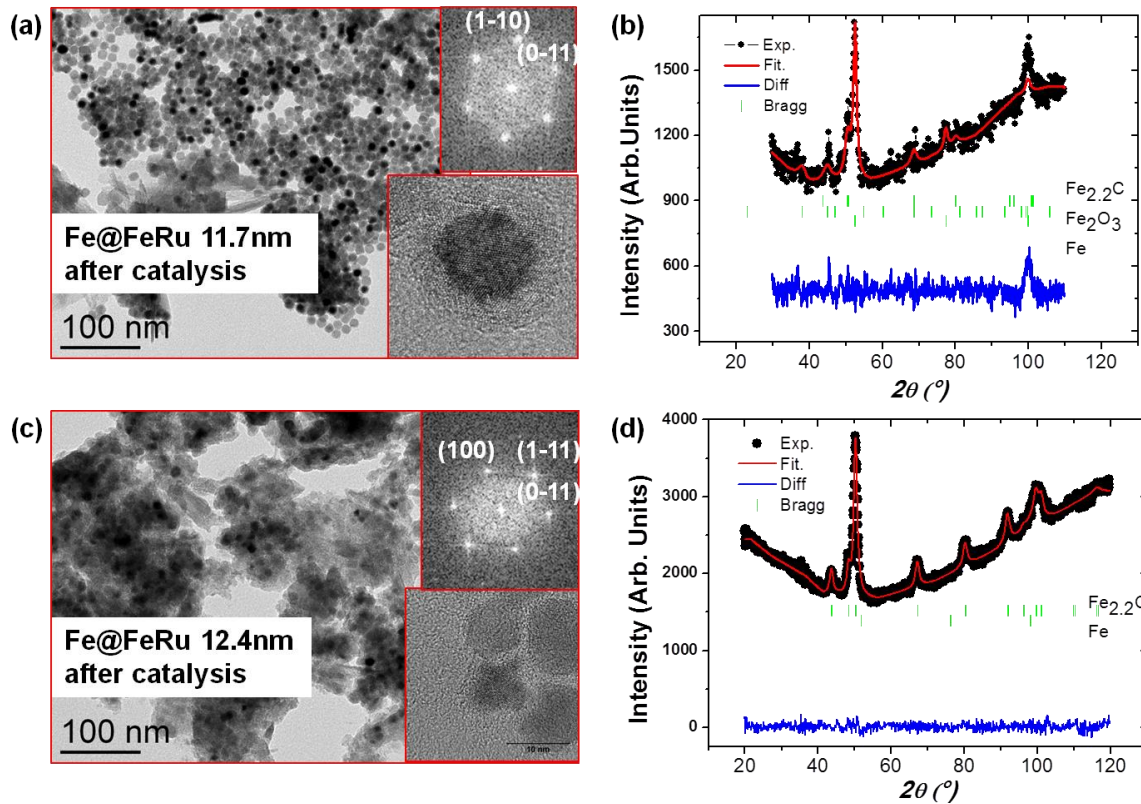


Figure 5: Two samples of Fe@Ru NPs after catalysis: (a) TEM, HRTEM of Fe@Ru (C) nanoparticles of about 11.7 nm after FTS; (b) DRX pattern of Fe@Ru (C) nanoparticles of about 11.7 nm after FTS; (c) TEM, HRTEM of Fe@Ru (C) nanoparticles of about 12.4 nm after FTS; (d) DRX pattern of Fe@Ru (C) nanoparticles of about 12.4 nm after FTS.

From the process and energetic point of views, as a result of the efficiency and rate of induction heating, the catalytic reaction starts instantaneously without any preliminary catalyst activation procedure. In our process, the magnetic field is generated using an air-cooled Litz wire coil, the energy consumption of which is much lower than standard water-cooled copper tube coils.³⁷ The coil presents a sample volume of 4 cm³ and an electrical power consumption when empty of approximately 400 W. The latter increases by 2 W when loaded with around 20 mg of magnetic material with a typical SAR of 100 W/g. Presently, the energy conversion ratio given by $2/(400+2) \approx 0.5\%$ is thus extremely small. If the same coil was filled with 10 % vol. of

nanoparticles (*ca.* 30 g), the ratio would reach $3000/(3000+400) \approx 88\%$, when neglecting skin depth effects.

Discussion and Conclusion

In summary, we report in this paper a proof of concept for high temperature magnetically induced heterogeneous catalysis applied to Fischer Tropsch Synthesis. The key point is the design of nanoparticles which combine high heating power and high surface activity. This was achieved by a method based on an organometallic approach deriving from the Fischer-Tropsch mechanism, through the reaction of carbonyl based precursors on metallic Fe seeds.³¹ It is first interesting to note that, in contrast to $\text{Fe}(\text{CO})_5$, the addition of $\text{Ru}_3(\text{CO})_{12}$ or $\text{Co}_2(\text{CO})_8$ to preformed $\text{Fe}(0)$ NPs at 150°C under H_2 does not lead to incorporation of carbon to form an iron carbide but preserves the $\text{Fe}(0)$ core. This is not due to a lack of reactivity of the NPs with CO since methane and higher hydrocarbons are produced. This, on the contrary, results from the onset of a fast catalytic formation of hydrocarbons, a process which prevents the incorporation of carbon into iron.

The three materials have been demonstrated to heat efficiently and display high SAR values under the application of a magnetic field of 50 mT at a frequency of 54 kHz, the Fe@Ru NPs displaying slightly lower values than the others at similar particle size as a result of the reduced surface magnetisation resulting from the Fe/Ru interface. The three materials were able to catalyse CO hydrogenation when exposed to an alternating magnetic field. The conditions used were voluntarily not those of real catalysis but used to test the propensity of these materials to perform catalysis and to deactivate. Quite astonishingly, the three systems work for Fischer-Tropsch synthesis and the presence of ruthenium, by increasing the catalytic activity and lowering the temperature, leads to an absence of deactivation, at least in the present conditions.

Nevertheless, even for the powder materials, which display relatively small SAR, the local surface temperature of the nanoparticles is most probably above 200°C to induce FTS, and probably more to induce some particle aggregation, while the outside surface of the reactor is not heated. Finally, direct inductive heating of nanoparticles combines heating simplicity and rapidity associated to energy efficiency. Furthermore, in our case, the presence of an optimized Litz-wire coil reduces considerably the global energetic input, and makes the local catalyst inductive heating very interesting in the context of intermittent power to gas conversion.

In conclusion, although we are far from any application, this study opens the door to : i) high temperature, magnetically induced, heterogeneous catalysis and ii) a fine tuning of catalytic properties and working temperatures through SAR control (e.g. size, shape, composition and chemical order, supporting material, nanoparticle density, ...) and surface loading with a pertinent catalytic metal. This very promising “cold magnetic catalysis” will be now developed in a context closer to real catalytic processes.

Supporting Information Available (10 pages):

Figure S1. (a) TEM micrographs of Fe(0) NPs used for the synthesis of bimetallic Fe@FeCo NPs. (b) size histogram of preformed Fe(0) NPs used for the synthesis of bimetallic Fe@FeCo NPs. (c) TEM micrographs of Fe(0) NPs for the synthesis of bimetallic Fe@Ru NPs. (d) size histogram of preformed Fe(0) NPs used for the synthesis of bimetallic Fe@Ru NPs. Figure S2. (a) Mass spectrum of gases produced during the synthesis of Fe@FeCo NPs. (b) Mass spectrum of gases produced during the synthesis of Fe@Ru NPs. Figure S3. (a) IR spectrum of Fe@Ru NPs before and after addition of CO. (b) IR spectrum of Fe(0) NPs before and after addition of CO. Figure S4. (a) TEM micrographs of Fe(0) NPs used for the synthesis of small bimetallic Fe@FeCo NPs of about 10.3. (b) Size histogram of Fe(0) NPs used for the synthesis of small

bimetallic Fe@FeCo NPs of about 10.3 nm. Figure S5. Structural analysis of small Fe@FeCo nanocrystals (**C**) of about 10.3 nm. (a), TEM analysis. (b), HRTEM analysis. (c), EDX data . (d), XRD pattern. (e), Mössbauer spectrum. Figure S6. (a) TEM micrographs of Fe(0) NPs used for the synthesis of small bimetallic Fe@Ru NPs of about 11.7 nm. (b) Size histogram of Fe(0) NPs used for the synthesis of small bimetallic Fe@Ru NPs of about 11.7 nm. Figure S7. Structural analysis of small Fe@Ru nanocrystals (**C**) of about 11.7 nm. (a), TEM analysis. (b), HRTEM analysis. (c), EDX data. (d), XRD pattern. (e), Mössbauer spectrum. Figure S8. (a) TEM micrographs of Fe(0) NPs used for the synthesis of small bimetallic Fe@Ru NPs of about 9.6 nm. (b) Size histogram of Fe(0) NPs used for the synthesis of small bimetallic Fe@Ru NPs of about 9.6 nm. Figure S9. Structural analysis of small Fe@Ru nanocrystals (**C**) of about 9.6 nm. (a), TEM analysis. (b), HRTEM analysis. (c), EDX data . (d), XRD pattern. Figure S10. Magnetization data analysis for Fe(0) (**A**). Figure S11. Magnetization data analysis for Fe@FeCo (**B**). Figure S12. Magnetization data analysis for Fe@Ru (**C**). Figure S13. Gas phase ^{13}C NMR of the gasses resulting from CO hydrogenation using Fe(0), Fe@FeCo and Fe@Ru as catalysts. Figure S14. Gas phase ^{13}C NMR of the gasses resulting from CO hydrogenation using Fe@Ru NPs of about 11.7 nm as catalysts. Figure S15. Gas phase ^{13}C NMR of the gasses resulting from CO hydrogenation using Fe@FeCo NPs of about 10.3 nm as catalysts. Figure S16. Analysis of Fe NPs after catalysis: (a) TEM analysis of Fe(0) NPs after catalysis. (b) HRTEM micrographs of Fe(0) NPs of about 10 nm after catalysis. (c) DRX pattern of Fe(0) NPs of about 10 nm after catalysis. Figure S17. Analysis of two samples of Fe@FeCo NPs after catalysis: (a) TEM, HRTEM of Fe@FeCo NPs of about 10.3 nm after FTS. (b) DRX pattern of Fe@FeCo NPs of about 10.3 nm after FTS. (c) TEM, HRTEM of Fe@FeCo (**B**) NPs of about 12.2 nm after FTS. (d) DRX pattern of Fe@FeCo. (**B**) NPs of about 12.2 nm after FTS. Table S1. Fitting parameters of the Mossbauer spectra collected at 4.2K, Isomer shift (IS), Quadrupolar splitting (Q),

hyperfine field ($\mu_0 H_{\text{Hyp}}$), linewidth (γ), and the quantification of each contribution (Contain).

Table S2. Structural and magnetic data of nanocatalysts before and after catalysis: TEM, HRTEM, EDX, SAR.

This material is available free of charge via the Internet at <http://pubs.acs.org>.

AUTHOR INFORMATION

Corresponding Author

*E-mail: bruno.chaudret@insa-toulouse.fr ; marc.respaud@insa-toulouse.fr

ACKNOWLEDGEMENTS

The authors thank ERC Advanced Grant (NANOSONWINGS 2009-246763) for financial support, LCC-CNRS Toulouse and J.-F. Meunier for magnetic (SQUID and Mössbauer) measurements, and CEMES-CNRS Toulouse for access to the high resolution transmission electronic platform.

Competing financial interests

The authors declare no competing financial interests.

References:

- (1) Schiermeier, Q. *Nature* **2013**, 496, 156-158
- (2) Khodakov, A.Y. ; Chu, W. ; Fongarland, P. *Chem. Rev.*, **2007**, 107, 1692-1744.
- (3) Bezemer, G.L.; Bitter, J.H.; Kuipers, H.P.C.E.; Osterbeek, H.; Holeyijn, J.E.; Xu, X.; Kapteijn, F.; Van Dillen, A.J.; de Jong, K.P. *J. Am. Chem. Soc.*, **2006**, 128, 3956-3964.
- (4) Chen, W.; Fan, Z.; Pan, X.; Bao, X. *J. Am. Chem. Soc.*, **2008**, 130, 9414-9419.
- (5) Xiao, C.; Cai, Z.; Wang, T.; Kou, Y.; Yan, N. *Angew. Chem. Int. Ed.*, **2008**, 47, 746-749.
- (6) Bao, J.; He, J.; Zhang, Y.; Yoneyama, Y.; Tsubaki, N. *Angew. Chem. Int. Ed.*, **2008**, 47, 353-356.
- (7) Quek, X.-Y.; Guan, Y.; van Santen, R. A.; Hensen, E. J. M., *ChemCatChem* **2011**, 3, 1735-1738.
- (8) Xiang, Y.; Chitry, V.; Liddicoat, P.; Felfer, P.; Cairney, J.; Ringer, S.; Kruse, N., Long- *J. Am. Chem. Soc.* **2013**, 135, 7114-7117.

- (9) Graham, U. M.; Jacobs, G.; Gnanamani, M. K.; Lipka, S. M.; Shafer, W. D.; Swartz, C. R.; Jermwongratanachai, T.; Chen, R.; Rogers, F.; Davis, B. H., *ACS Catalysis* **2014**, 1662-1672.
- (10) Liu, J. J.; Guo, Z.; Childers, D.; Schweitzer, N.; Marshall, C. L.; Klie, R. F.; Miller, J. T.; Meyer, R. J., *J. Catal.* **2014**, 313, 149-158.
- (11) G. Benkowsky, Induktionserwärmung: Härten, Glühen, Schmelzen, Löten, Schweißen: Grundlagen und praktische Anleitungen für Induktionserwärmungsverfahren, insbesondere auf dem Gebiet der Hochfrequenzerwärmung, 5th ed., Verlag Technik, Berlin, **1990**, p. 12.
- (12) Kirschning, A.; Kupracz, L.; Hartwig, J. *Chem. Lett.*, **2012**, 41, 562–570.
- (13) Ceylan, S.; Friese, C.; Lammel, C.; Mazac, K.; Kirschning, A.; *Angew. Chem. Int. Ed.*, **2008**, 47, 8950-8953.
- (14) Ceylan, S.; Coutable, L.; Wegner, J.; Kirschning, A. *Chem. Eur. J.* **2011**, 17, 1884–1893
- (15) Hartwig, J.; Ceylan, S.; Kupracz, L.; Coutable, L.; Kirschning, A. *Angew. Chem. Int. Ed.* **2013**, 52, 9813 –9817.
- (16) N’Guyen, T. T. T.; Duong, H. T. T.; Basuki, J.; Montembault, V.; Pascual, S.; Guibert, C.; Fresnais, J.; Boyer, C.; Whittaker, M. R.; Davis, T. P.; *Angew. Chem. Int. Ed.*, **2013**, 52, 14152–14156.
- (17) Riedinger, A.; Guardia, P.; Curcio, A.; Garcia, M. A.; Cingolani, R.; Manna, L.; Pellegrino, T. *Nano Lett.* **2013**, 13, 2399–2406.
- (18) Dias, J. T.; Moros, M.; del Pino, P.; Rivera, S.; Grazú, V.; de la Fuente, J. M. *Angew. Chem. Int. Ed.* **2013**, 55, 11526–11529.
- (19) Polo-Corrales, L.; Rinaldi, C. *J. Appl. Phys.*, **2012**, 111, 07B334.
- (20) Huang, H.; Delikanli, S.; Zeng, H.; Ferkey, D. M.; Pralle, A. *Nat. Nanotech.* **2010**, 5, 602–606.
- (21) Creixell, M.; Bohorquez, A. C.; Torres-Lugo, M.; Rinaldi, C., *ACS Nano* **2011**, 5, 7124–7129.
- (22) Kellner, C.S.; Bell, A.T. *J. Catal.* **1982**, 75, 251-261.
- (23) Kang, J.; Zhang, S.; Zhang, Q.; Wang, Y. *Angew. Chem. Int. Ed.*, **2009**, 48, 2565-2568.
- (24) Carballo, J.M.G.; Yang, J.; Holmen, A.; Garcia-Rodriguez, S.; Rojas, S.; Ojeda, M.; Fierro, J.L.G. *J. Catal.*, **2011**, 284, 102-108.
- (25) Torres Galvis, H.M.; Bitter, J.H.; Davidian, T.; Ruitenbeek, M.; Dugulan, A.I.; de Jong, K.P. *J. Am. Chem. Soc.*, **2012**, 134, 16207-16215.
- (26) Torres Galvis, H.M.; Bitter, J.H.; Khare, C.B.; Ruitenbeek, M.; Dugulan, A.I.; de Jong, K.P. *Science*, **2012**, 335, 835-838.
- (27) Borg, O.; Dietzel, P.D.C.; Spjelkavik, A.I.; Tveten, E.Z.; Walmsley, J.C.; Dislas, S.; Eri, S.; Holmen, A.; Rytter, E. *J. Catal.*, **2008**, 259, 161-164.
- (28) Dumestre, F. ; Chaudret, B. ; Amiens, C. ; Renaud, P. ; Fejes, P. *Science*, **2004**, 303, 821-823.
- (29) Lacroix, L.-M.; Lachaize, S. ; Falqui, A. ; Respaud, M. ; Chaudret, B. *J. Am. Chem. Soc.* **2009**, 131, 549-557.
- (30) Lacroix, L.-M.; Bel-Malaki, R.; Carrey, J.; Lachaize, S.; Goya, G. F.; Chaudret, B.; Respaud, M. *J. Appl. Phys.* **2009** 105, 023911.
- (31) Mehdaoui, B.; Meffre, A.; Carrey, J.; Lachaize, S.; Lacroix, L. M.; Gougeon, M.; B. Chaudret, B.; Respaud, M. *Adv. Func. Mater.* **2011**, 21, 4573-4581.
- (32) Meffre, A.; Mehdaoui, B.; Kelsen, V.; Fazzini, P.F.; Carrey, J.; Lachaize, S.; Respaud, M.; Chaudret, B. *Nano Lett.* **2012**, 12, 4722-4728.
- (33) Meffre, A.; Lachaize, S.; Gatel, C.; Respaud, M.; Chaudret, B. *J. Mater. Chem.*, **2011**, 21, 13464-13469.

- (34) Desvaux, C.; Lecante, P.; Respaud, M.; Chaudret, B. *J. Mater. Chem.*, **2010**, 20, 103-109.
- (35) Kobayashi, M ; Ando, N ; Kai, TS ; Takano, N ; Shiiki, K ; *J. Phys.-Cond. Mat.*, **1995**, 7, 9607-9614.
- (36) Mehdaoui, B. ; Tan, R.P. ; Meffre, A. ; Carrey, J. ; Lachaize, S. ; Chaudret, B. ; Respaud, M. *Phys. Rev. B* **2013**, 87, 174419.
- (37) Connord V. ; Mehdaoui B. ; Tan R.P. ; Carrey J. ; Respaud M. *Rev. Sci. Instr.* **2014**, 85, 093904.

Table of Contents

